

# All-scale hierarchical thermoelectrics: MgTe in PbTe facilitates valence band convergence and suppresses bipolar thermal transport for high performance†

Cite this: *Energy Environ. Sci.*, 2013, **6**, 3346

L. D. Zhao,<sup>a</sup> H. J. Wu,<sup>b</sup> S. Q. Hao,<sup>c</sup> C. I. Wu,<sup>d</sup> X. Y. Zhou,<sup>e</sup> K. Biswas,<sup>a</sup> J. Q. He,<sup>\*b</sup> T. P. Hogan,<sup>d</sup> C. Uher,<sup>e</sup> C. Wolverton,<sup>c</sup> V. P. Dravid<sup>c</sup> and M. G. Kanatzidis<sup>\*a</sup>

We report a high  $ZT$  of  $\sim 2.0$  at 823 K for 2% Na-doped PbTe with 6% MgTe with excellent thermal stability. We attribute the high thermoelectric performance to a synergistic combination of enhanced power factor, reduction of the lattice thermal conductivity and simultaneous suppression of bipolar thermal conductivity. MgTe inclusion in PbTe owns triple functions: the Mg alloying within the solubility limit in PbTe modifies the valence band structure by pushing the two valence bands (L and  $\Sigma$  bands) closer in energy, thereby facilitating charge carrier injection. When the solubility limit of Mg is exceeded, ubiquitous endotaxial nanostructures form, which when coupled with mesoscale microstructuring results in a very low (lattice) thermal conductivity through all-scaled length phonon scattering. Meanwhile, most significantly, the Mg alloying enlarges the energy gap of conduction band (C band) and light valence band (L band), thereby suppresses the bipolar thermal conductivity through an increase in band gap.

Received 29th June 2013

Accepted 11th September 2013

DOI: 10.1039/c3ee42187b

[www.rsc.org/ees](http://www.rsc.org/ees)

## Environmental impact

Bipolar thermal conductivity contributes significantly to the total thermal conductivity in bulk thermoelectrics at elevated (operating) temperatures; thereby compromising the  $ZT$  in important thermoelectric materials such as PbTe. Since the band gap in PbTe is only about 0.3 eV, elevated temperatures promote minority carrier jumps across the band gap and the diffusing electron-hole pair gives rise to this additional thermal conductivity contribution, which limits the  $ZT$  at high temperatures. Any mechanisms to suppress it would signal a new approach to reduce thermal conductivity, thus increase  $ZT$ . Indeed, herein we show that through the addition of Mg alloying on the Pb sites of PbTe moves the light and heavy valence bands closer together. This leads to an enhancement of the Seebeck coefficient because two bands are contributing. From the homologous group of MgTe, CaTe, SrTe, BaTe, only MgTe has this effect! We explain this theoretically in our contribution. The combination of Mg alloying on the Pb sites with excess MgTe forming nanostructures in the PbTe matrix leads to a bipolar thermal conductivity suppression and thermal conductivity reduction. Thus, the enhancement of the Seebeck coefficient, the suppression of bipolar thermal transport and the reduction of lattice thermal conductivity together help to achieve a  $ZT$  value of 2.0 at 823 K.

<sup>a</sup>Department of Chemistry, Northwestern University, Evanston, Illinois 60208, USA. E-mail: m-kanatzidis@northwestern.edu

<sup>b</sup>Department of Physics, South University of Science and Technology of China, Shenzhen 518055, China. E-mail: he.jq@sustc.edu.cn

<sup>c</sup>Department of Materials Science and Engineering, Northwestern University, Evanston, Illinois 60208, USA

<sup>d</sup>Department of Electrical and Computer Engineering, Michigan State University, East Lansing, Michigan 48824, USA

<sup>e</sup>Department of Physics, University of Michigan, Ann Arbor, Michigan, 48109, USA

† Electronic supplementary information (ESI) available: Experimental details and characterizations; calculation of lattice thermal conductivity; density of samples included in the study (Table S1); input parameters for calculation of relaxation time of phonon scattering for  $\text{Pb}_{0.98}\text{Na}_{0.02}\text{Te} + 6\%$  MgTe (Table S2); heat capacity, thermal diffusivity, Lorenz number and electronic thermal conductivity as a function of temperature for  $\text{Pb}_{0.98}\text{Na}_{0.02}\text{Te} + 6\%$  MgTe (Fig. S1); the band structure calculations for PbTe,  $\text{Pb}_{0.99}\text{Mg}_{0.01}\text{Te}$  and  $\text{Pb}_{0.96}\text{Mg}_{0.04}\text{Te}$  (Fig. S2); low-magnification TEM image (Fig. S3); thermoelectric properties as a function of temperature for five  $\text{Pb}_{0.98}\text{Na}_{0.02}\text{Te} + 6\%$  MgTe samples and one sample annealed at 873 K for 2 weeks (Fig. S4); TEM images for  $\text{Pb}_{0.98}\text{Na}_{0.02}\text{Te} + 6\%$  MgTe sample annealed at 873 K for 2 weeks (Fig. S5). See DOI: 10.1039/c3ee42187b

## Introduction

Thermoelectric power generation technology is a type of solid-state ‘heat engine’ that is capable of converting heat to electricity. The efficiency of thermoelectric materials is determined by the dimensionless figure of merit,  $ZT = (S^2\sigma/\kappa)T$ , where  $S$ ,  $\sigma$ ,  $\kappa$ , and  $T$  are the Seebeck coefficient, electrical conductivity, thermal conductivity, and absolute temperature, respectively.<sup>1,2</sup> The interdependent nature of  $S$ ,  $\sigma$  and  $\kappa$  complicates efforts in developing strategies for improving a material's  $ZT$  above 3, a feat that could revolutionize the field of energy conversion. In the past decades, persistent efforts have been made to enhance  $ZT$  through either lowering thermal conductivity ( $\kappa$ ) or boosting power factor ( $S^2\sigma$ ). The most successful route has been to reduce the thermal conductivity, particularly through nanostructuring. Typical examples are embedding nanoscale precipitates in parent materials that scatter heat-carrying phonons.<sup>3–9</sup> Alternatively, the power factor can be improved by increasing Seebeck coefficients without significantly diminishing electrical

conductivity through modifying band structure by band engineering,<sup>10,11</sup> quantum confinement designing<sup>12</sup> and electron energy barrier filtering.<sup>13</sup>

Among the materials suitable for power generation applications, PbTe has an exceptional base thermoelectric performance. Great progress has recently been made to obtain high  $ZT$  in PbTe-based materials using nanostructuring group II tellurides (MgTe, CaTe, SrTe and BaTe). These nanostructured precipitates facilitate broad-based phonon scattering while allowing good carrier transport between the endotaxially aligned components, thus minimizing significant deterioration of the hole mobility.<sup>3,14–16</sup> In heavily doped p-type PbTe, the contributions from valence bands (L and  $\Sigma$  bands) enhance the Seebeck coefficient and the power factor.<sup>11,17</sup> We propose that alloying of the PbTe matrix may result in tuning of the relative energies of the L and  $\Sigma$  bands to accomplish a more controllable convergence with respect to temperature; for example, Mg alloying in PbTe may make the energy difference between L and  $\Sigma$  bands to decrease with respect to the alloying fractions.<sup>18,19</sup> In contrast to the endotaxial CaTe, SrTe and BaTe nanoparticles which have very small solubility and mainly form secondary phases in PbTe, MgTe was found to be the only group II telluride with substantial solid-state solubility in PbTe matrix.<sup>19</sup> Ohta *et al.*<sup>16</sup> and Pei *et al.*<sup>18</sup> reported excellent performance in PbTe system  $ZT \sim 1.6$  peaks at 780 K and  $ZT \sim 1.7$  peaks at 750 K using MgTe, respectively. However, both these studies reported MgTe solubility fractions only up to 3%, below the expected solubility limit of MgTe in PbTe.<sup>19</sup>

Here we report that when larger fractions of MgTe are added in the PbTe matrix significantly higher thermoelectric performance can be achieved. This happens because (a) the Seebeck coefficients are enhanced by decreasing the energy difference of the two valence bands (L and  $\Sigma$  bands). The other congeners CaTe, SrTe and BaTe do not exhibit this effect. MgTe alloying does so by pushing the two bands closer together within the solubility limit ( $\sim 4\%$ ); (b) an additional thermal conductivity reducing mechanism appears; that of suppression of the bipolar thermal conductivity, which boosts the  $ZT$  to  $\sim 2.0$  at 823 K. Our results further show that band structure tailoring to enhance the Seebeck coefficient is independent of mechanisms for phonon scattering, implying that power factor enhancement and reduction in thermal conductivity can work with remarkable synergy.

## Experimental

Starting materials are Pb wire (99.99%, American Elements, US), Te shot (99.999%, 5 N Plus, Canada), Mg (99.98%, Sigma-Aldrich, US) and Na chunk (99.999%, Sigma-Aldrich, US). Ingots ( $\sim 20$  g) with nominal compositions of  $Pb_{1-x}Mg_xTe$  ( $x = 0, 0.01, 0.02, 0.04, 0.05, 0.06$  and  $0.08$ ) and with 2.0% Na dopant (mol fraction in the text) were synthesized by mixing appreciated ratios of high purity starting materials in  $\varnothing \sim 8$  mm carbon coating silica tubes of under an  $N_2$ -filled glove box. The tubes were then evacuated to a pressure of  $\sim 10^{-4}$  torr, flame-sealed, slowly heated to 723 K in 12 h, then to 1423 K in 7 h, soaked at this temperature for 6 h and subsequently air quenched to room temperature. The obtained

ingots were crushed into powders and then densified by spark plasma sintering (SPS) method (SPS-10-4, Thermal Technology LLC), highly dense samples can achieve  $>97\%$  of theoretical density. The experimental details for SPS processing, annealing treatments, density of samples included in the study, thermoelectric properties measurements, band gap measurements, Hall measurements, electron microscopy, X-ray diffraction, calculation of the relaxation time of phonon scattering and band structure calculations can be found in ESI.†

## Results and discussion

### Solid solution limit of MgTe in PbTe

Powder XRD patterns of  $Pb_{0.98}Na_{0.02}Te + x\%$  MgTe samples show a single phase that can be indexed to the NaCl structure type up to 8% MgTe, Fig. 1(a). No MgTe or other phases were observed within the detection limits of the measurements. A control sample  $Pb_{0.98}Na_{0.02}Te$  was also prepared for comparison. As shown in Fig. 1(b), the lattice parameter decreases with increasing Mg fraction, consistent with the smaller radius of  $Mg^{2+}$  ( $\sim 0.86$  Å) compared to that of  $Pb^{2+}$  ( $\sim 1.19$  Å). The lattice parameter decreases significantly up to 4% MgTe and beyond that shows a negligible change (see deviation from Vegard's law type behavior, dashed line in Fig. 1(b)) as the content reaches 8%. With increasing MgTe fraction the electronic absorption spectra of the PbTe samples (without Na doping) show a shift of the absorption edge towards higher energy, Fig. 1(c). The band gaps derived from the plots show an increase from  $\sim 0.30$  eV to  $\sim 0.40$  eV in going from 1% to 4% MgTe in PbTe. Beyond this fraction the band gaps show negligible changes as the MgTe fraction reaches 8%. Generally, if MgTe were forming solid solution with PbTe, one would expect a sustained Vegard's law type behavior, showing systematic increase in band gap with MgTe amount ( $E_{g,MgTe} \sim 3\text{--}5$  eV), Fig. 1(d). The increase in the band gap is observed only up to 4% fraction. It suggests that at  $>4\%$  MgTe is excluded from the PbTe matrix. Collectively, both the lattice parameter and band gap variations suggest that the solubility limit is somewhere around 4% MgTe.

### Thermoelectric transport properties

Fig. 2 shows the thermoelectric properties as a function of temperature for  $Pb_{0.98}Na_{0.02}Te + x\%$  MgTe. The electrical conductivities decrease with increasing temperature, Fig. 2(a), and are lower for increasing amounts of MgTe over the entire temperature range. Specifically, the room temperature electrical conductivity significantly decreases from  $\sim 2406$  S  $cm^{-1}$  for  $Pb_{0.98}Na_{0.02}Te$  to  $\sim 984$  S  $cm^{-1}$  for the sample with 8% MgTe. From 0 to 4% MgTe the hole mobility diminishes only slightly, but above this fraction and up to 8% MgTe the mobility falls significantly, Table 1. Interestingly, the same trend is also observed in the carrier concentration dependence on MgTe fractions. As shown in Fig. 2(b), the Seebeck coefficients are positive, and show an increasing trend with increasing temperature. It is worth noting that Seebeck coefficients at room temperature also show an increasing trend with increasing MgTe fractions. It is readily seen that the Seebeck coefficient reaches a

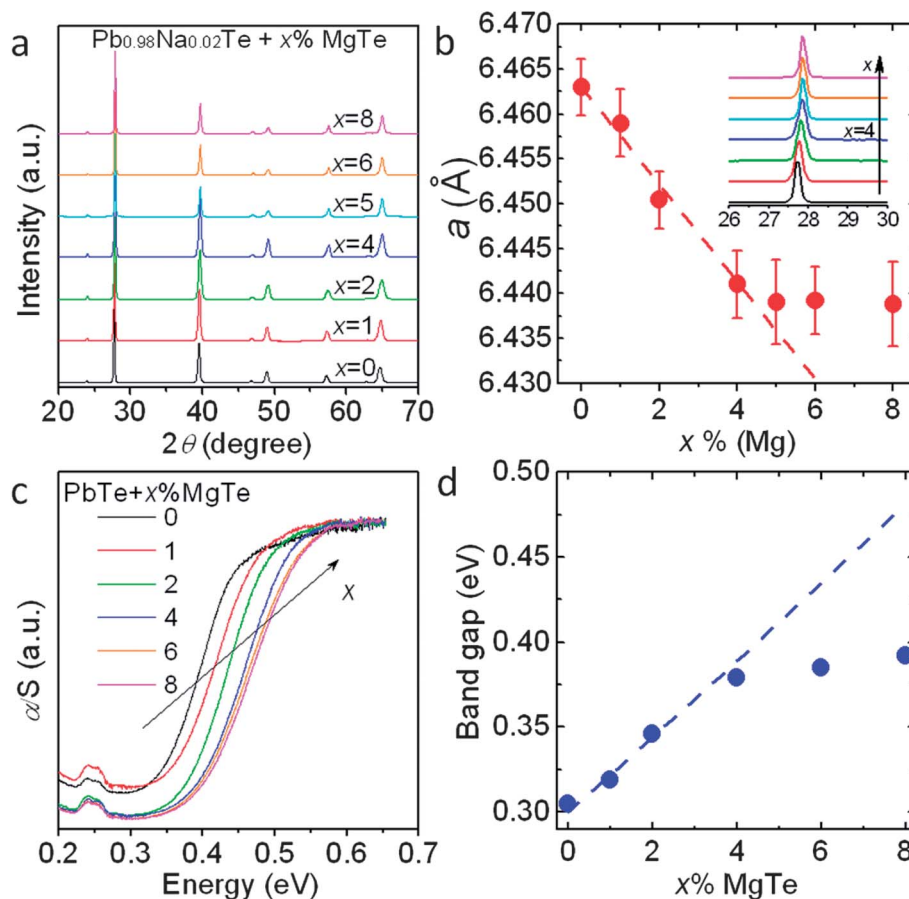


**Fig. 1** The solubility limit of MgTe in PbTe. (a) Powder XRD patterns and (b) Lattice parameter (the inset shows the enlarged XRD peaks shifting) for  $\text{Pb}_{0.98}\text{Na}_{0.02}\text{Te} + x\%$  MgTe. (c) Electronic absorption spectra and (d) band gap variation for  $\text{PbTe} + x\%$  MgTe. The behaviors for both lattice parameter and band gap deviate from Vegard's law dotted lines in (b) and (d) indicate a  $\sim 4\%$  Mg solubility limit in PbTe.

maximum at around 750 K for  $\text{Pb}_{0.98}\text{Na}_{0.02}\text{Te}$ . The Seebeck coefficient peak (with temperature) is a sign of an onset of bipolar diffusion as intrinsic carriers are excited across the energy gaps of PbTe. This onset is also reflected in the thermal conductivity (discussed later). The bipolar diffusion adversely affects the Seebeck coefficient due to a rising contribution of minority carriers and an increased activation energy at elevated temperatures. For samples with up to 4% MgTe, the widened band gap from  $\sim 0.30$  to  $\sim 0.40$  eV can suppress bipolar diffusion. For all MgTe containing samples, the Seebeck coefficient maxima shift to higher temperature with rising MgTe fractions, but no Seebeck coefficient saturation (onset of bipolar diffusion) was observed at  $>4\%$  MgTe up to 923 K. This observation is consistent with the relationships of band gap ( $E_g$ ), the maximum Seebeck coefficient ( $S_{\text{max}}$ ) and the temperature  $T_{\text{max}}$  at which the  $S_{\text{max}}$  occurs:  $E_g = 2eS_{\text{max}}T_{\text{max}}$ , where  $e$  is the electron charge.<sup>20</sup> The power factor of the control sample  $\text{Pb}_{0.98}\text{Na}_{0.02}\text{Te}$  sample peaks at  $\sim 28 \mu\text{W cm}^{-1} \text{K}^{-2}$  around 600 K falling to  $\sim 20 \mu\text{W cm}^{-1} \text{K}^{-2}$  at 923 K, Fig. 2(c). It is readily seen that the power factors at 923 K have been enhanced by introducing MgTe, ranging from  $\sim 20 \mu\text{W cm}^{-1} \text{K}^{-2}$  for  $\text{Pb}_{0.98}\text{Na}_{0.02}\text{Te}$  sample to  $\sim 25 \mu\text{W cm}^{-1} \text{K}^{-2}$  for 2% MgTe containing sample.

The total thermal conductivity ( $\kappa_{\text{tot}}$ ) shows a significant decrease with increasing MgTe, Fig. 2(d).  $\kappa_{\text{tot}}$  is the sum of the

electronic ( $\kappa_{\text{ele}}$ ) and lattice thermal conductivity ( $\kappa_{\text{lat}}$ ).  $\kappa_{\text{ele}}$  is proportional to the electrical conductivity ( $\sigma$ ) through the Wiedemann–Franz relation,  $\kappa_{\text{ele}} = L\sigma T$ , where  $L$  is the Lorenz number. Due to the complexity and the non-parabolicity of the valence band structure around the Fermi level for p-type PbTe, accurate determination of the  $L$  is difficult. An estimation of  $L$  can be made using a single parabolic band (SPB) model with acoustic phonon scattering<sup>6,7,21</sup> resulting in an  $L$  with a deviation of less than 10% as compared with a more rigorous single non-parabolic band and multiple band models calculation.<sup>22</sup> Heat capacity, thermal diffusivity, Lorenz number and electronic thermal conductivity for  $\text{Pb}_{0.98}\text{Na}_{0.02}\text{Te} + x\%$  MgTe are shown in Fig. S1.†

The total thermal conductivity shows a significant decrease with increasing MgTe, and this trend is also observed in the lattice thermal conductivity, Fig. 2(e). This reduction in lattice thermal conductivity indicates that the well-dispersed nano-structured MgTe is highly effective in phonon scattering. At room temperature the lattice thermal conductivity decreases from  $\sim 2.83 \text{ W m}^{-1} \text{K}^{-1}$  for  $\text{Pb}_{0.98}\text{Na}_{0.02}\text{Te}$  to  $\sim 1.50 \text{ W m}^{-1} \text{K}^{-1}$  for the  $\text{Pb}_{0.98}\text{Na}_{0.02}\text{Te} + 8\%$  MgTe. Correspondingly, the lattice thermal conductivity at 923 K decreases from  $\sim 1.38 \text{ W m}^{-1} \text{K}^{-1}$  for  $\text{Pb}_{0.98}\text{Na}_{0.02}\text{Te}$  to  $\sim 0.53 \text{ W m}^{-1} \text{K}^{-1}$  for 8% MgTe sample. In Fig. 2(e), the lattice thermal conductivity for  $\text{Pb}_{0.98}\text{Na}_{0.02}\text{Te} + 6\%$

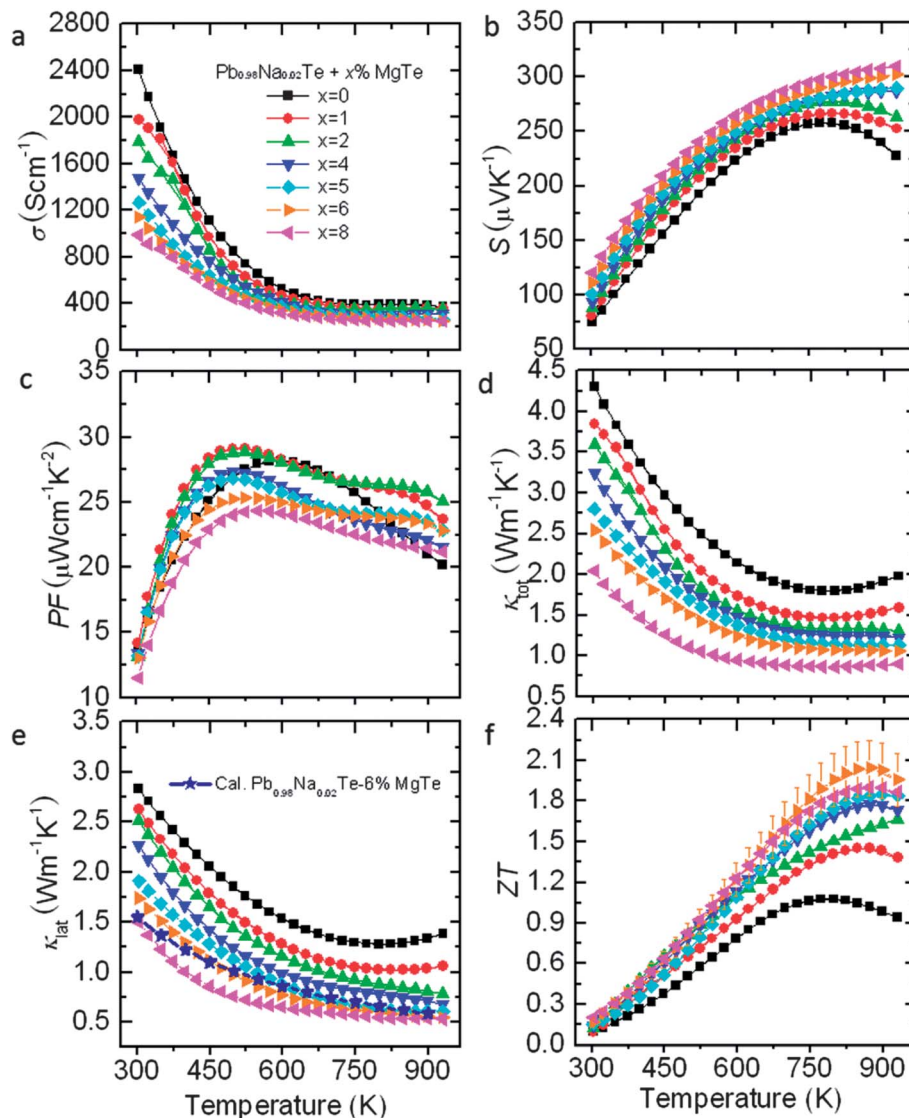


**Fig. 2** Thermoelectric properties as a function of temperature for  $\text{Pb}_{0.98}\text{Na}_{0.02}\text{Te} + x\% \text{MgTe}$ . (a) Electrical conductivity. (b) Seebeck coefficient. (c) Power factor. (d) Total thermal conductivity. (e) Lattice thermal conductivity and the calculation for  $\text{Pb}_{0.98}\text{Na}_{0.02}\text{Te} + 6\% \text{MgTe}$ . (f) Figure of merit,  $ZT$ , the combined uncertainty for all measurements involved in the calculation of  $ZT$  is less than 15%.

$\text{MgTe}$  has been calculated based on the modified Callaway model (details in ESI<sup>†</sup>), which shows good agreement with experimental values. While both experiments and calculations

indicate that the nanoscale precipitates play a dominant role in reducing the lattice thermal conductivity, point defects and mesoscale grain boundaries can further reduce the lattice

**Table 1** Transport properties of  $\text{Pb}_{0.98}\text{Na}_{0.02}\text{Te} + x\% \text{MgTe}$ <sup>a</sup>

Samples	$n_{\text{H}}$ ( $10^{20} \text{ cm}^{-3}$ )	$r_{\text{H}}$	$\mu_{\text{H}}$ ( $\text{cm}^2 \text{ V}^{-1} \text{ s}^{-1}$ )	$S$ ( $\mu\text{V K}^{-1}$ )	$\sigma$ ( $\text{S cm}^{-1}$ )	$m^*(m_e)$	$\kappa_{\text{L}}$ (RT) ( $\text{W m}^{-1} \text{ K}^{-1}$ )	$\kappa_{\text{L}}$ (923 K) ( $\text{W m}^{-1} \text{ K}^{-1}$ )	$ZT_{\text{max}}$
$\text{Pb}_{0.98}\text{Na}_{0.02}\text{Te}$	1.21	1.05	95	74	2406	0.85	2.83	1.38	1.1
$\text{Pb}_{0.98}\text{Na}_{0.02}\text{Te} + 1\% \text{MgTe}$	1.11	1.06	93	80	1981	0.98	2.62	1.05	1.4
$\text{Pb}_{0.98}\text{Na}_{0.02}\text{Te} + 2\% \text{MgTe}$	1.02	1.06	90	88	1785	1.15	2.51	0.78	1.6
$\text{Pb}_{0.98}\text{Na}_{0.02}\text{Te} + 4\% \text{MgTe}$	1.01	1.06	91	95	1477	1.20	2.27	0.68	1.7
$\text{Pb}_{0.98}\text{Na}_{0.02}\text{Te} + 5\% \text{MgTe}$	0.92	1.07	86	100	1267	1.19	1.90	0.61	1.8
$\text{Pb}_{0.98}\text{Na}_{0.02}\text{Te} + 6\% \text{MgTe}$	0.87	1.09	82	111	1142	1.18	1.74	0.54	2.0
$\text{Pb}_{0.98}\text{Na}_{0.02}\text{Te} + 8\% \text{MgTe}$	0.88	1.09	70	120	984	1.21	1.50	0.53	1.9

<sup>a</sup>  $n_{\text{H}}$ , carrier concentration;  $r_{\text{H}}$ , Hall factor;  $\mu_{\text{H}}$ , carrier mobility;  $S$ , Seebeck coefficient;  $\sigma$ , electrical conductivity;  $m^*(m_e)$ , the effective mass;  $\kappa_{\text{L}}$ , lattice thermal conductivity;  $ZT$ , the dimensionless figure of merit.

thermal conductivity. As shown in Fig. 2(f), the  $ZT$  value of  $\sim 2.0$  at 823 K is reached for the  $\text{Pb}_{0.98}\text{Na}_{0.02}\text{Te} + 6\%$  MgTe sample. This high performance also shows a good experimental repeatability and thermal stability, Fig. S2 and S3.†

### Role of Mg in enhancement of Seebeck coefficients *via* heavy valence band convergence

The carriers in heavily doped p-type PbTe are distributed into two different valence bands, which occur at the L point (L band) and along the  $\Sigma$  line ( $\Sigma$  band) in the Brillouin zone,<sup>17,23</sup> having an energy offset at low temperature. As the temperature increases, the L band gradually lowers its energy and passes the  $\Sigma$  band edge at a specific temperature point which is dependent on the energy offsets between L and  $\Sigma$  bands. When the two valence bands convergence, the Seebeck coefficient can be enhanced by increasing the effective mass  $m^*$  by a factor of  $N_v^{2/3}$ ,  $N_v$  is the number of degeneracy valleys,  $N_v$  is 4 for L band and increases to 12 for the  $\Sigma$  band.<sup>14,17</sup> Specifically,  $m^* = N_v^{2/3} m_b^*$ , where  $m_b^*$  is the average (single valley) effective mass of the degenerate valleys. Mg alloying in PbTe can have a similar effect of altering the energies of both L and  $\Sigma$  bands.

We use density functional theory (DFT) calculations to investigate the effect of MgTe alloying in PbTe on the conduction and valence bands (L and  $\Sigma$  bands). We use rock salt supercells of PbTe and different dilute concentrations of Mg

additions at  $\sim 1.0\%$  ( $\text{Pb}_{124}\text{Mg}_1\text{Te}_{125}$ ) and  $\sim 4.0\%$  ( $\text{Pb}_{26}\text{Mg}_1\text{Te}_{27}$ ). The calculations were performed using the generalized gradient approximation Perdew–Burke–Ernzerhof (PBE) exchange function<sup>24</sup> with projector augmented-wave (PAW) potentials<sup>25</sup> as implemented in VASP (Vienna Ab-initio Simulation Package).<sup>26</sup> After relaxation, the energy level of L-point and  $\Sigma$ -line and corresponding energy differences are calculated. The actual DFT calculation band structures for PbTe,  $\text{Pb}_{0.99}\text{Mg}_{0.01}\text{Te}$  and  $\text{Pb}_{0.96}\text{Mg}_{0.04}\text{Te}$  are shown in Fig. S4.† As shown in Fig. 3(a), schematically, the conduction band (C) shows negligible energy change with Mg fraction, however, the valence bands (L and  $\Sigma$ ) drop in energy relative to the conduction band. The addition of Mg results in decreasing energy offsets between L and  $\Sigma$  bands, Fig. 3(b). These changes in the calculated band structure with alloying are also experimentally confirmed by Hall measurements, Fig. 3(c). A maximum  $R_H$  is a sign of convergence of the two valence bands (L and  $\Sigma$  bands).

The well-established Pisarenko relation between the Seebeck coefficient and carrier concentration<sup>10</sup> gives a good description of the experimental data, Fig. 3(d). The black solid line is the theoretical Pisarenko line corresponding to a single parabolic band with the assumption of acoustic phonon scattering.<sup>10,18–21</sup> Alloying with increasing concentration of Mg increases the band-gap energy between L and C bands ( $\Delta E_{C-L}$ ), which is consistent with the band gap measurements. Meanwhile, the energy of the  $\Sigma$  band remains roughly constant with respect to

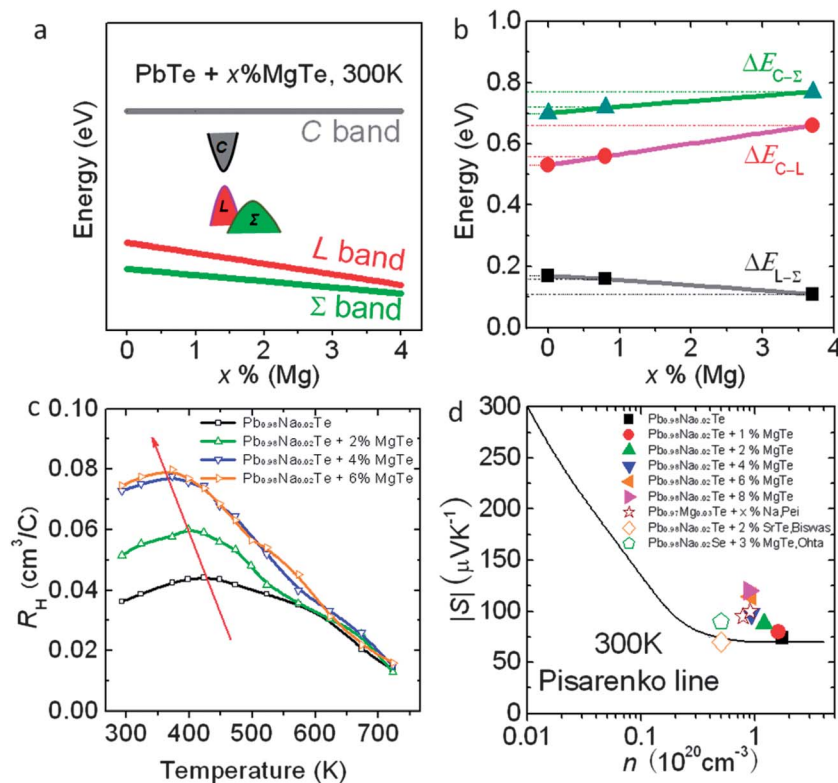


**Fig. 3** Band engineering of Mg alloyed PbTe. (a) Conduction band (C band) and valence bands (L and  $\Sigma$  bands) and (b) their energy differences as a function of Mg fractions in PbTe. (c) Hall coefficients as a function of temperature for  $\text{Pb}_{0.98}\text{Na}_{0.02}\text{Te} + x\%$  MgTe and (d) Pisarenko plots at 300 K, the black solid line is the theoretical Pisarenko line that takes into account the valence band structure of PbTe. Mg alloying in PbTe increased the valence bands energy, lowered the energy offsets between L and  $\Sigma$  bands, pushed the Hall coefficient maxima shifting to lower temperature, resulting in enhancement of Seebeck coefficients which are above the Pisarenko line.

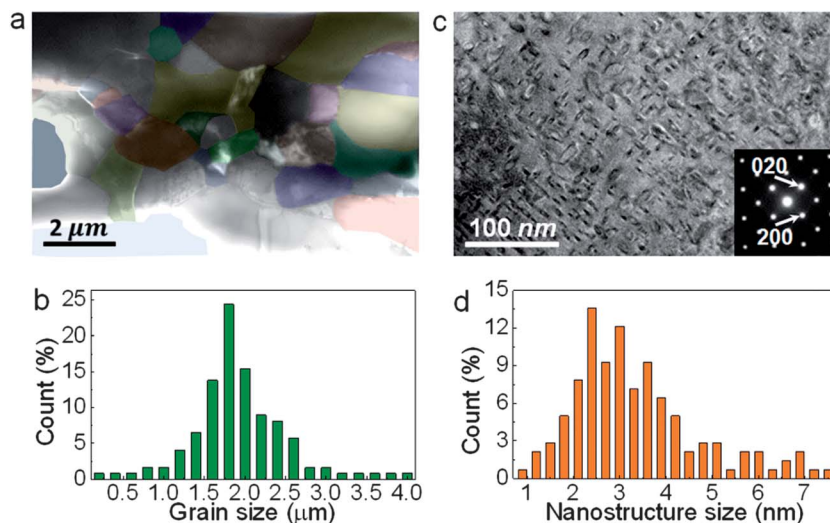


**Fig. 4** Microstructures of  $\text{Pb}_{0.98}\text{Na}_{0.02}\text{Te} + 6\% \text{MgTe}$ . (a) Low-magnification TEM image reveals mesoscale grains. (b) Grain size distribution histogram. (c) Medium-magnification TEM image shows presence of platelet-like and spherical/ellipsoidal nanoscale precipitates. (d) Precipitate size distribution histogram. The inset electron diffraction pattern in (c) confirms the crystallographic alignment of MgTe in the PbTe.

the C band. It can be noticed that Mg alloying brings the two valence bands L and  $\Sigma$  closer in energy ( $\Delta E_{L-\Sigma}$ ) which decreases the convergence temperature for L and  $\Sigma$  bands, resulting in an increase of effective mass at a lower temperature than that in the absence of MgTe (Table 1). Essentially, this amounts to an increase in the density of state (DOS) near the Fermi energy and can account for the enhanced Seebeck coefficient lying well above the Pisarenko line.

### All length-scale hierarchical structuring

In this section, we describe the detailed microstructure of the  $\text{Pb}_{0.98}\text{Na}_{0.02}\text{Te} + 6\% \text{MgTe}$  sample, studied by means of transmission electron microscopy (TEM). The presence of mesoscale grains around  $1.8 \mu\text{m}$  ( $0.1\text{--}4.0 \mu\text{m}$  in size) is evident in Fig. 4(a) and (b). Nanoscale precipitates around  $5 \text{ nm}$  ( $1\text{--}8 \text{ nm}$  in size) appearing as platelet-like and spherical/ellipsoidal are shown in Fig. 4(c) and (d). The inset electron diffraction pattern with the electron beam along the  $[001]$  zone axis shown in Fig. 4(c) confirms the endotaxial crystallographic alignment of MgTe precipitates with the PbTe matrix. The projection traces of the nanoscale precipitates direct along  $[100]$  and  $[010]$ , Fig. 4(c). The precipitates growing in the preferred direction reflect anisotropic morphology. Smaller precipitates with platelet-like shape are typically coherently strained, reflecting elastic accommodation of an interfacial misfit, while larger precipitates with spherical or ellipsoidal shape exhibit interfacial misfit dislocations due to excess coherency strain.<sup>3,15,27</sup>

Scanning TEM (STEM) in combination with energy dispersive X-ray spectroscopy (EDS) can be used to compare the Mg concentration in the precipitates with that in the matrix of  $\text{Pb}_{0.98}\text{Na}_{0.02}\text{Te} + 6\% \text{MgTe}$ . Although it is complicated to quantitatively determine the exact compositions of individual precipitates because of their overlap with the matrix, Fig. 5(a), EDS can still qualitatively indicate a large increase in the Mg signal from the precipitates (blue areas in the inset STEM

image) compared with matrix regions (red areas in the inset STEM image), which suggests that the precipitates are mainly MgTe. Fig. 5(b) shows a representative high-resolution TEM (HRTEM) image of platelet-like precipitates obtained with the electron beam along the  $[001]$  zone axis for  $\text{Pb}_{0.98}\text{Na}_{0.02}\text{Te} + 6\% \text{MgTe}$ . The inset Fast Fourier Transform (FFT) image in the inset confirms the endotaxial alignment of the MgTe precipitates with the PbTe matrix. All platelet-like precipitates are organized perpendicular or parallel to each other, consistent with two of three possible crystallographic directions.<sup>3</sup>

To analyze the possible strain around the platelet-like precipitates, the high-quality HRTEM images were analyzed by geometric phase analysis (GPA),<sup>28,29</sup> which is a semi-quantitative lattice image-processing approach for revealing spatial distribution of relative elastic strain. Fig. 5(c) shows an enlarged image and its analyzed GPA results, namely the component  $\varepsilon_{xx}$  and  $\varepsilon_{yy}$  of the strain. The image shows one platelet-like precipitate enclosed by dotted lines, and its plate plane is parallel with the direction of electron beam. GPA images indicate that there is elastic strain only along the plate plane ( $\varepsilon_{yy}$ ). The strain distribution in platelet-like precipitates is anisotropic, in contrast to spherical/ellipsoidal precipitates, which have isotropic strain distributions.<sup>3,15</sup>

Fig. 5(d) shows a lattice image of two neighboring grains and their interfacial region. The corresponding low-magnification image of Fig. 5(d) is shown in Fig. S5.† To investigate the interfacial region, secondary phases or overlapping of grain boundaries, we analyze the crystallographic relationship of such boundary with upper and lower grains. The FFT image-processing was carried out to identify the observation direction of selected upper grain area and lower grain area as  $[001]$  and  $[012]$  zone axis, respectively. The interfacial area shows two sets of the crystallographic orientations with a relationship of  $220^{[001]}/200^{[012]}$  which means this region probably involves the overlapping of two grains. Fig. 5(e) shows a high magnification image with overlapped grain boundary between  $[001]$  and  $[012]$

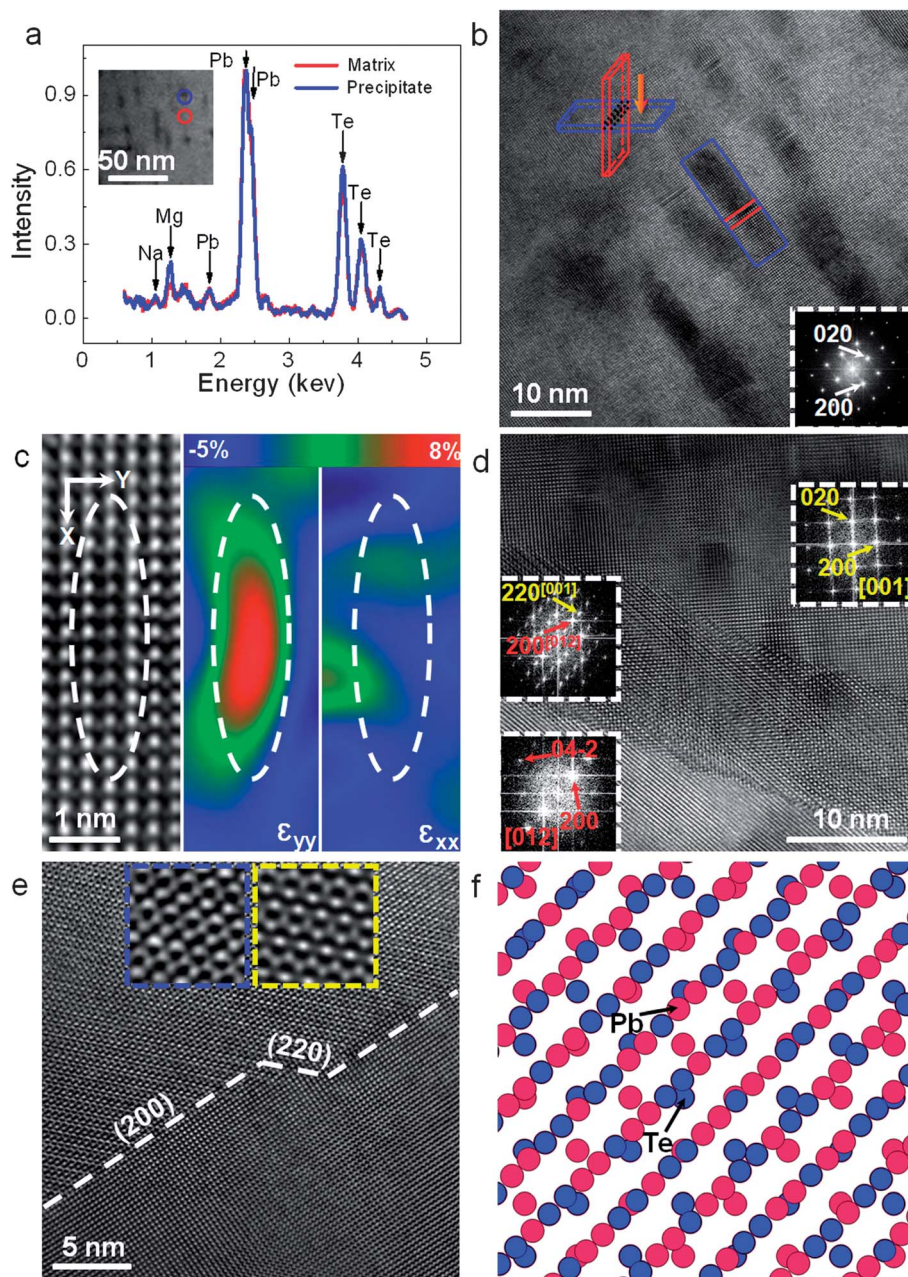


**Fig. 5** Compositional analysis and nanostructures of  $\text{Pb}_{0.98}\text{Na}_{0.02}\text{Te} + 6\% \text{MgTe}$ . (a) EDS spectra for typical precipitate (blue) and matrix (red) in the sample (STEM image, insert). (b) Lattice image depicts plate-like precipitates, an inset schematic of the corresponding precipitate morphology in 3 dimensional space reflects two plate-like precipitates perpendicular to each other, and the arrowhead indicates the direction of the TEM observations. (c) Lattice image and strain maps shows elastic strain (color scale) along the direction of platelet-like precipitate. (d) Lattice image shows two grains with interfacial layer, the inset FFT images show the observation directions. (e) Lattice image depicts the  $[001]$  grain and the interfacial layer sharing  $(200)$  and  $(220)$  planes (red dashed lines), inset enlarged lattice image of interfacial layer (blue dashed lines) and inset corresponding simulated lattice image (yellow dashed lines) based on atomic model in (f). (f) The corresponding atomic structural model of the interfacial layer.

grains. The shared planes between the overlapped (upper) area and lower area are along  $(220)$  and  $(200)$  marked with white dashed lines. In order to further identify the overlapping region, we use Crystallite software to establish a modeling of the overlapping boundary of two grains with a relationship of  $220^{[001]}/200^{[012]}$ , and then use Mactempas to simulate the high-magnification lattice image (inset image marked with yellow dashed lines) based on the atomic structural model of the interfacial

layer, Fig. 5(f). The experimental (marked with blue dashed lines in Fig. 5(e)) and simulated images are in agreement with each other. The above analysis can exclude the argument of second phase. In addition, the  $[001]/[012]$  grain boundary is widespread in  $\text{Pb}_{0.98}\text{Na}_{0.02}\text{Te} + 6\% \text{MgTe}$ , that means preferred grain growth. Considering the above three main mechanisms revealed by TEM, the lattice thermal conductivity of  $\text{Pb}_{0.98}\text{Na}_{0.02}\text{Te} + 6\% \text{MgTe}$  based on modified Callaway model

was calculated (details in ESI†). The results are shown in Fig. 2(e), under the margin of error 10%, match the experimental data reasonably well for temperatures between 300 and 900 K.

### Suppression of bipolar thermal conductivity

In the intrinsic conduction region for narrow-band-gap semiconductors, such as  $\text{Bi}_2\text{Te}_3$  system,<sup>21</sup> a considerable contribution to the thermal conductivity is made by the component due to the ambipolar diffusion of electrons and holes. This significant component to the total thermal conductivity is the so-called bipolar thermal conductivity. Besides the contribution to total thermal conductivity, bipolar effects also degrade Seebeck coefficients, because minority carriers, thermally excited across the band gap, have Seebeck coefficients with the opposite sign, and will offset that of the majority ones. Therefore, bipolar effects will limit the  $ZT$  at higher temperatures. The bipolar effect happens even at 300 K in  $\text{Bi}_2\text{Te}_3$  system due to small band gap of 0.13 eV.<sup>21</sup> In the  $\text{Bi}_2\text{Te}_3$  system, the bipolar effects can be suppressed by either increasing majority carrier concentrations through heavy doping<sup>30</sup> or building up energy barrier filters through nanosized grains.<sup>31</sup>

Since the band gap in PbTe is about 0.30 eV, a rising temperature promotes minority carrier jumps across the band

gap and the diffusing electron-hole pair gives rise to an additional thermal conductivity contribution. In this paper we present an effective way to suppress the bipolar thermal conductivity by increasing the band gap from 0.30 eV to 0.40 eV through Mg alloying in PbTe. This is in stark contrast to the SrTe system where is due to the very low solubility in PbTe exhibits no energy gap widening and no substantial bipolar suppression. If bipolar diffusion takes place, the lattice thermal conductivity  $\kappa_{\text{lat}}$  can be overestimated since an extra term (bipolar thermal conductivity,  $\kappa_{\text{bi}}$ ) contributes to the total thermal conductivity. At high temperature the minority carriers generated in intrinsic excitations not only decrease the Seebeck coefficient, but also increase the thermal conductivity due to the bipolar diffusion. Therefore, the total thermal conductivity  $\kappa_{\text{tot}}$  is given by:<sup>32</sup>

$$\kappa_{\text{tot}} = \kappa_{\text{lat}} + \kappa_{\text{ele}} + \kappa_{\text{bi}} \quad (1)$$

In order to clarify the contribution of bipolar thermal conductivity  $\kappa_{\text{bi}}$  at high temperature, the  $\kappa_{\text{bi}}$  is separated from the  $\kappa_{\text{tot}}$  according to the proposed method.<sup>33,34</sup> The difference,  $\kappa_{\text{tot}} - \kappa_{\text{ele}}$ , as a function of  $T^{-1}$  for the lead chalcogenides is shown in Fig. 6(a). Since the acoustic phonon scattering is predominant at low temperatures before bipolar diffusion is significant,<sup>17</sup>  $\kappa_{\text{tot}} - \kappa_{\text{ele}}$  equals to  $\kappa_{\text{lat}}$ , which is proportional to  $T^{-1}$ . The lattice thermal conductivity can be approximately given:<sup>32</sup>

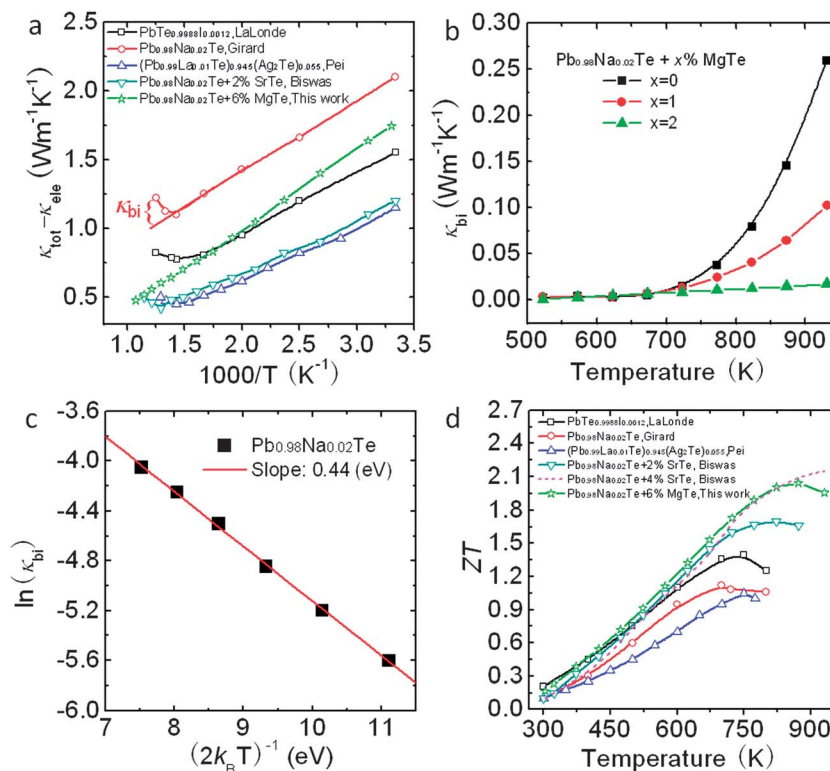


**Fig. 6** Bipolar thermal conductivity and ZT. (a) The difference of total and electronic thermal conductivity ( $\kappa_{\text{tot}} - \kappa_{\text{ele}}$ ) as a function of temperature for PbTe system, the solid line is linearly fitting to the lattice thermal conductivity at temperature ranges from room temperature to 923 K, deviation of thermal conductivity indicates a significant bipolar thermal conductivity. (b) Bipolar thermal conductivity as a function of temperature for  $\text{Pb}_{0.98}\text{Na}_{0.02}\text{Te} + x\%$  MgTe. (c) Plot of  $\ln(\kappa_{\text{bi}})$  vs.  $1/(2k_{\text{B}}T)$  for  $\text{Pb}_{0.98}\text{Na}_{0.02}\text{Te}$  to derive the bipolar diffusion energy. (d) Figure of merit ( $ZT$ ) comparisons. Mg alloying in PbTe suppressed the bipolar diffusion and pushed the ZT shifting to high temperature.  $\text{PbTe}_{0.9988}\text{I}_{0.0012}$  (black square),<sup>36</sup>  $\text{Pb}_{0.98}\text{Na}_{0.02}\text{Te}$  (red circle),<sup>35</sup>  $(\text{Pb}_{0.99}\text{La}_{0.01}\text{Te})_{0.945}(\text{Ag}_2\text{Te})_{0.055}$  (blue upwards triangle),<sup>37</sup>  $\text{Pb}_{0.98}\text{Na}_{0.02}\text{Te} + 2\%$  SrTe (dark green downwards triangle),<sup>15</sup> and  $\text{Pb}_{0.98}\text{Na}_{0.02}\text{Te} + 4\%$  SrTe (pink dotted line)<sup>3</sup> are listed for comparison.

$$\kappa_{\text{lat}} = 3.5 \left( \frac{k_{\text{B}}}{h} \right)^3 \frac{MV^{1/3} \theta_{\text{D}}^3}{\gamma^2 T} \quad (2)$$

where the  $k_{\text{B}}$  is the Boltzmann's constant,  $h$  the Planck constant,  $M$  the average mass per atom,  $V$  the average atomic volume,  $\theta_{\text{D}}$  the Debye temperature, and  $\gamma$  the Grüneisen parameter. As shown in Fig. 6(a), as the temperature is increased to  $\sim 650$  K, the  $\kappa_{\text{tot}} - \kappa_{\text{ele}}$  starts to gradually deviate from a linear relationship between  $\kappa_{\text{lat}}$  and  $T^{-1}$  because the bipolar diffusion starts to contribute to the thermal conductivity. The  $\kappa_{\text{bi}}$  at high temperatures was estimated by extrapolating the linear relationship between  $\kappa_{\text{lat}}$  and  $T^{-1}$ , as indicated by the solid line in Fig. 6(a). For example,  $\kappa_{\text{bi}}$  can be observed in  $\text{Pb}_{0.98}\text{Na}_{0.02}\text{Te}$ ,<sup>35</sup>  $\text{PbTe}_{0.9988}\text{I}_{0.0012}$ ,<sup>36</sup>  $(\text{Pb}_{0.99}\text{La}_{0.01}\text{Te})_{0.945}(\text{Ag}_2\text{Te})_{0.055}$ ,<sup>37</sup> and  $\text{Pb}_{0.98}\text{Na}_{0.02}\text{Te} + 2\%$  SrTe.<sup>15</sup> However, for the  $\text{Pb}_{0.98}\text{Na}_{0.02}\text{Te} + 6\%$  MgTe sample, we observe no departure from the linear dependence at high temperature in Fig. 6(a). This is due to the increased band gap and therefore the diminished bipolar contribution with increasing Mg alloying fractions in PbTe, Fig. 6(b).

For a narrow-band-gap semiconductor, the energy required for bipolar diffusion should be higher than the band gap. The energy for bipolar diffusion can be roughly estimated from the relationship:<sup>38</sup>

$$\kappa_{\text{bi}} = A \exp\left(\frac{-E_{\text{g}}^*}{2k_{\text{B}}T}\right) \quad (3)$$

where  $A$  is a constant,  $E_{\text{g}}^*$  is the band gap for the bipolar diffusion. Here, we make a plot of  $\ln(\kappa_{\text{bi}})$  vs.  $1/(2k_{\text{B}}T)$  for  $\text{Pb}_{0.98}\text{Na}_{0.02}\text{Te}$  without Mg alloying, along with a fit to the above equation that yields a energy of  $E_{\text{g}}^* \sim 0.44$  eV, as shown in Fig. 6(c). This means that the bipolar diffusion happens at  $\sim 650$  K, the energy is required to be more than 0.44 eV, which is comparable to the band gap of PbTe at  $\sim 650$  K. In other words, the band gap of PbTe increases from 0.30 eV at 300 K to 0.44 eV at 650 K. The band gap of  $\text{Pb}_{0.98}\text{Na}_{0.02}\text{Te} + 6\%$  MgTe at 650 K is estimated at  $\sim 0.54$  eV; this energy is higher than that required for bipolar diffusion at this temperature. Hence, the suppression of bipolar diffusion significantly contributes to the higher  $ZT$  for  $\text{Pb}_{0.98}\text{Na}_{0.02}\text{Te} + 6\%$  MgTe sample compared to other PbTe systems,<sup>15,35–37</sup> see Fig. 6(d). In the MgTe case we observe a slightly lower power factor than the SrTe case,<sup>3</sup> namely, the power factor at 910 K is  $\sim 25 \mu\text{W cm}^{-1} \text{K}^{-2}$  for  $\text{Pb}_{0.98}\text{Na}_{0.02}\text{Te} + 4\%$  SrTe vs.  $\sim 22 \mu\text{W cm}^{-1} \text{K}^{-2}$  for  $\text{Pb}_{0.98}\text{Na}_{0.02}\text{Te} + 6\%$  MgTe. The valence band alignment in the case of MgTe is not as good as that in the SrTe system as suggested by the lower hole mobilities ( $86$  vs.  $99 \text{ cm}^2 \text{V}^{-1} \text{s}^{-1}$  respectively).<sup>15</sup> This results in a  $ZT \sim 2.0$  for  $\text{Pb}_{0.98}\text{Na}_{0.02}\text{Te} + 6\%$  MgTe vs.  $2.2$  for  $\text{Pb}_{0.98}\text{Na}_{0.02}\text{Te} + 4\%$  SrTe at 923 K but the MgTe system outperforms the SrTe system in the temperature range from 300 to 823 K.

## Concluding remarks

Mg alloying has three main effects on PbTe: (a) brings the two valence bands (L and  $\Sigma$ ) closer in energy ( $\Delta E_{\text{L}-\Sigma}$ ) by lowering both energies which contributes to the enhancement of the Seebeck coefficient; (b) increases the PbTe band gap which suppresses the

bipolar thermal conductivity at high temperature; (c) produces ubiquitous nanostructuring that appears as Mg exceeds the solubility limit. Meanwhile, favorable microscaled grain structures are obtained through spark plasma sintering completing the all length-scale hierarchical structuring which significantly reduces the lattice thermal conductivity. The integration of these effects in a single material pushes  $ZT$  to 2.0 at 823 K.

## Acknowledgements

This work was supported in part by a grant DOE-EERE/NSF (CBET-1048728) (LDZ and MGK). Work at SUSTC was also supported by SUSTC Startup funding (JQH). The spark plasma sintering and density functional calculations in this work were supported as part of the Revolutionary Materials for Solid State Energy Conversion, an Energy Frontier Research Center funded by the U.S. Department of Energy, Office of Science, and Office of Basic Energy Sciences under Award Number DE-SC0001054 (CIW, SQH, XZ, CU, CW, TPH and VPD). We acknowledge use of the Office of Naval Research DURIP-supported Spark Plasma Sintering System at Michigan State University. Transmission electron microscopy work was partially performed in the (EPIC) (NIFTI) (Keck-II) facility of NUANCE Center at Northwestern University.

## References

- (a) M. G. Kanatzidis, *Chem. Mater.*, 2010, **22**, 648–659; (b) J. He, M. G. Kanatzidis and V. P. Dravid, *Mater. Today*, 2013, **16**, 166–176.
- (a) J. F. Li, W. S. Liu, L. D. Zhao and M. Zhou, *NPG Asia Mater.*, 2010, **2**, 152–158; (b) A. J. Minnich, M. S. Dresselhaus, Z. F. Ren and G. Chen, *Energy Environ. Sci.*, 2009, **2**, 466–479; (c) J. Baxter, Z. X. Bian, G. Chen, D. Danielson, M. S. Dresselhaus, A. G. Fedorov, T. S. Fisher, C. W. Jones, E. Maginn, U. Kortshagen, A. Manthiram, A. Nozik, D. R. Rolison, T. Sands, L. Shi, D. Sholl and Y. Wu, *Energy Environ. Sci.*, 2009, **2**, 559–588.
- K. Biswas, J. He, I. D. Blum, C. Wu, T. Hogan, D. N. Seidman, V. P. Dravid and M. G. Kanatzidis, *Nature*, 2012, **489**, 414–418.
- J. Q. He, S. N. Girard, M. G. Kanatzidis and V. P. Dravid, *Adv. Funct. Mater.*, 2010, **20**, 764–772.
- (a) K. F. Hsu, S. Loo, F. Guo, W. Chen, J. S. Dyck, C. Uher, T. Hogan, E. K. Polychroniadis and M. G. Kanatzidis, *Science*, 2004, **303**, 818–821; (b) E. Quarez, K. F. Hsu, R. Pcionek, N. Frangis, E. K. Polychroniadis and M. G. Kanatzidis, *J. Am. Chem. Soc.*, 2005, **127**, 9177–9190; (c) D. Bilc, S. D. Mahanti, K. F. Hsu, E. Quarez, R. Pcionek and M. G. Kanatzidis, *Phys. Rev. Lett.*, 2004, **93**, 146403.
- L. D. Zhao, J. Q. He, S. Q. Hao, C. I. Wu, T. P. Hogan, C. Wolverton, V. P. Dravid and M. G. Kanatzidis, *J. Am. Chem. Soc.*, 2012, **134**, 16327–16336.
- L. D. Zhao, J. Q. He, C. I. Wu, T. P. Hogan, X. Y. Zhou, C. Uher, V. P. Dravid and M. G. Kanatzidis, *J. Am. Chem. Soc.*, 2012, **134**, 7902–7912.
- (a) M. Zhou, J. F. Li and T. Kita, *J. Am. Chem. Soc.*, 2008, **130**, 4527–4532; (b) X. B. Zhao, X. H. Ji, Y. H. Zhang, T. J. Zhu, J. P. Tu and X. B. Zhang, *Appl. Phys. Lett.*, 2005, **86**, 062111.

- 9 S. V. Barabash, V. Ozolins and C. Wolverton, *Phys. Rev. Lett.*, 2008, **101**, 15.
- 10 (a) J. P. Heremans, V. Jovic, E. S. Toberer, A. Saramat, K. Kurosaki, A. Charoenphakdee, S. Yamanaka and G. J. Snyder, *Science*, 2008, **321**, 554–557; (b) J. P. Heremans, B. Wiendlocha and A. M. Chamoire, *Energy Environ. Sci.*, 2012, **5**, 5510–5530.
- 11 (a) Y. Z. Pei, X. Y. Shi, A. LaLonde, H. Wang, L. D. Chen and G. J. Snyder, *Nature*, 2011, **473**, 66–69; (b) Y. Z. Pei, A. LaLonde, S. Iwanaga and G. J. Snyder, *Energy Environ. Sci.*, 2011, **4**, 2085–2089.
- 12 T. C. Harman, P. J. Taylor, M. P. Walsh and B. E. LaForge, *Science*, 2002, **297**, 2229–2232.
- 13 J. P. Heremans, C. M. Thrush and D. T. Morelli, *Phys. Rev. E: Stat., Nonlinear, Soft Matter Phys.*, 2004, **70**, 115334.
- 14 K. Biswas, J. Q. He, G. Y. Wang, S. H. Lo, C. Uher, V. P. Dravid and M. G. Kanatzidis, *Energy Environ. Sci.*, 2011, **4**, 4675–4684.
- 15 K. Biswas, J. Q. He, Q. C. Zhang, G. Y. Wang, C. Uher, V. P. Dravid and M. G. Kanatzidis, *Nat. Chem.*, 2011, **3**, 160–166.
- 16 M. Ohta, K. Biswas, S. H. Lo, J. Q. He, D. Y. Chung, V. P. Dravid and M. G. Kanatzidis, *Adv. Energy Mater.*, 2012, **2**, 1117–1123.
- 17 I. I. Ravich, B. A. Efimova and I. A. Smirnov, *Semiconducting Lead Chalcogenides*, Plenum Press, New York, 1970.
- 18 Y. Z. Pei, A. D. LaLonde, N. A. Heinz, X. Y. Shi, S. Iwanaga, H. Wang, L. D. Chen and G. J. Snyder, *Adv. Mater.*, 2011, **23**, 5674–5678.
- 19 L. M. Rogers and A. J. Crocker, *J. Phys. D: Appl. Phys.*, 1971, **4**, 1006–1015.
- 20 X. Shi, J. Y. Cho, J. R. Salvador, J. Yang and H. Wang, *Appl. Phys. Lett.*, 2010, **96**, 16.
- 21 D. M. Rowe, *CRC Handbook of Thermoelectrics*, CRC Press, 1995.
- 22 I. A. Smirnov, Mn. Vinograd, Nv. Kolomoet and L. M. Sysoeva, *Soviet Physics – Solid State*, 1968, **9**, 2074–2079.
- 23 C. M. Jaworski, M. D. Nielsen, H. Wang, S. N. Girard, W. Cai, W. D. Porter, M. G. Kanatzidis and J. P. Heremans, *Phys. Rev. B*, 2013, **87**, 045203.
- 24 J. P. Perdew, K. Burke and M. Ernzerhof, *Phys. Rev. Lett.*, 1996, **77**, 3865–3868.
- 25 P. E. Blochl, *Phys. Rev. B: Condens. Matter Mater. Phys.*, 1994, **50**, 17953–17979.
- 26 G. Kresse and J. Furthmuller, *Phys. Rev. B: Condens. Matter Mater. Phys.*, 1996, **54**, 11169–11186.
- 27 J. W. Doak and C. Wolverton, *Phys. Rev. B: Condens. Matter Mater. Phys.*, 2012, **86**, 14.
- 28 J. Q. He, E. Vasco, C. L. Jia and R. H. Wang, *Appl. Phys. Lett.*, 2005, **87**, 062901.
- 29 M. J. Hÿtch, E. Snoeck and R. Kilaas, *Ultramicroscopy*, 1998, **74**, 131–146.
- 30 H. J. Goldsmid, *Proc. Phys. Soc., London*, 1958, **71**, 633–646.
- 31 B. Poudel, Q. Hao, Y. Ma, Y. Lan, A. Minnich, B. Yu, X. Yan, D. Wang, A. Muto, D. Vashaee, X. Chen, J. Liu, M. S. Dresselhaus, G. Chen and Z. F. Ren, *Science*, 2008, **320**, 634–638.
- 32 G. S. Nolas and H. J. Goldsmid, in *Thermal Conductivity-2003: Theory, Properties and Applications*, ed. T. M. Tritt, Kluwer Academic, New York, 2004, 1(4), pp. 105–121.
- 33 H. Kitagawa, M. Wakatsuki, H. Nagaoka, H. Noguchi, Y. Isoda, K. Hasezaki and Y. Noda, *J. Phys. Chem. Solids*, 2005, **66**, 1635–1639.
- 34 W. S. Liu, B. P. Zhang, J. F. Li, H. L. Zhang and L. D. Zhao, *J. Appl. Phys.*, 2007, **102**, 103717.
- 35 S. N. Girard, J. He, X. Zhou, D. Shoemaker, C. M. Jaworski, C. Uher, V. P. Dravid, J. P. Heremans and M. G. Kanatzidis, *J. Am. Chem. Soc.*, 2011, **133**, 16588–16597.
- 36 A. D. LaLonde, Y. Pei and G. J. Snyder, *Energy Environ. Sci.*, 2011, **4**, 2090–2096.
- 37 Y. Pei, J. Lensch-Falk, E. S. Toberer, D. L. Medlin and G. J. Snyder, *Adv. Funct. Mater.*, 2011, **21**, 241–249.
- 38 O. C. Yelgel and G. P. Srivastava, *Phys. Rev. E: Stat., Nonlinear, Soft Matter Phys.*, 2012, **85**, 12.